

# UDC: Unified DNAS for Compressible TinyML Models

Igor Fedorov  
ARM ML Research Lab  
igor.fedorov@arm.com

Ramon Matas  
ARM ML Research Lab  
ramon.matas@arm.com

Hokchhay Tann  
ARM ML Research Lab  
hokchhay.tann@arm.com

Chuteng Zhou  
ARM ML Research Lab  
chu.zhou@arm.com

Matthew Mattina\*  
Tenstorrent  
mmattina77@gmail.com

Paul Whatmough  
ARM ML Research Lab  
paul.whatmough@arm.com

## Abstract

Emerging Internet-of-things (IoT) applications are driving deployment of neural networks (NNs) on heavily constrained low-cost hardware (HW) platforms, where accuracy is typically limited by memory capacity. To address this TinyML challenge, new HW platforms like neural processing units (NPUs) have support for model compression, which exploits aggressive network quantization and unstructured pruning optimizations. The combination of NPUs with HW compression and compressible models allows more expressive models in the same memory footprint.

However, adding optimizations for compressibility on top of conventional NN architecture choices expands the design space across which we must make balanced trade-offs. This work bridges the gap between NPU HW capability and NN model design, by proposing a neural architecture search (NAS) algorithm to efficiently search a large design space, including: network depth, operator type, layer width, bitwidth, sparsity, and more. Building on differentiable NAS (DNAS) with several key improvements, we demonstrate *Unified DNAS for Compressible models (UDC)* on CIFAR100, ImageNet, and DIV2K super resolution tasks. On ImageNet, we find Pareto dominant compressible models, which are  $1.9\times$  smaller or 5.76% more accurate.

## 1. Introduction

In TinyML applications, we seek to design machine learning (ML) models that run on highly-constrained hardware (HW) platforms with limited memory and compute capabilities [12]. Canonical examples of TinyML tasks include visual wakewords, audio keyword spotting, anomaly detection, speech enhancement, and image classification [7, 11, 12, 24, 41]. To meet the tight energy and cost chal-

Table 1. Overview of UDC characteristics vs prior NAS.

	MCUNet [41]	APQ [56]	HAQ [55]	Yang et al. [58]	Gong et al. [26]	Choi et al. [17]	Uhlich et al. [53]	UDC (Ours)
Width + Operator + Depth Search	✓	✓						✓
Bitwidth + Sparsity Search				✓		✓		✓
Guaranteed to meet HW constraint	✓	✓		✓	✓		✓	✓
Deployable w/ Integer Math Only	✓	✓			✓	✓	✓	✓

lenges of TinyML, HW vendors have begun offering neural processing units (NPUs), which are processors specialized for neural network (NN) inference [1, 2]. Model Compression is an important feature of NPUs, allowing NN weights to be stored in a reduced (compressed) memory footprint by exploiting low entropy weight distributions enhanced with sparsity and quantization. This compressed model is then decompressed by the NPU at inference time. HW model compression offers an enormous advantage in the TinyML setting, where limited Flash memory is often the main bottleneck to increasing model accuracy. [23, 41]. Secondly, a smaller memory footprint also reduces memory access energy at inference time [9, 30, 38], which can be very significant for battery powered IoT devices [4].

When deploying NN inference on conventional microcontroller units (MCUs), the software (SW) inference runtime (e.g. Tensor Flow Lite Micro (TFLM) [5] or uTensor [6]) only support 8-bit quantization, with no model compression. Thus, quantization below 8-bit does not reduce the deployed model size. Similarly, unstructured pruning [30] does not benefit inference on MCUs, as there is neither HW or SW support for compression or sparse math [5, 6]. In contrast, NPUs with HW support for compressed models allow us to benefit from both sub-byte quantization and unstructured pruning [3]. For example, Fig. 2 shows how model size scales with quantization, pruning, and both, when compressed for deployment using the Vela NPU com-

\*Work done while at ARM ML Research Lab

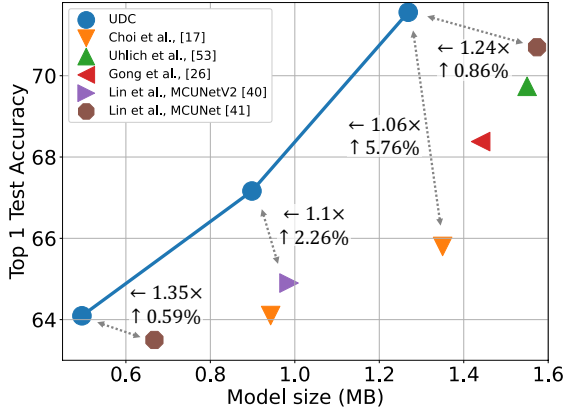


Figure 1. ImageNet test set accuracy vs. compressed model size.

piler [3], down to a  $9.3\times$  reduction in model size for 1-bit quantization and 1% non-zero weights in the extreme.

Given the ability to efficiently deploy compressed NNs on NPU, the question then becomes how to design compressible models. Constructing bit-efficient NNs that balance all available architectural choices and optimizations is arduous, as the design space is vast. This space can be divided into two parts: 1) the NN architecture itself, designed using neural architecture search (NAS) for layer widths [18, 24, 31, 46, 54, 57, 59, 60], network operators, depth, and connectivity [12, 16, 21, 23, 41], and 2) optimizations, such as per-layer quantization bitwidth [53, 55, 56, 58, 61], and unstructured weight pruning<sup>1</sup> [17, 29, 30, 37, 42].

For NPU deployment, there are two additional considerations. First, commercial NPUs [2] only support 8-bit integer convolutions [2], hence, non-uniform floating-point quantization [55, 58] is not viable. Second, HW memory is finite, so it is essential to have a hard constraint on the model size, rather than merely regularizing the size, since the latter does not necessarily guarantee that the models found fit into the allotted memory. Existing NAS approaches lack one or more of the aforementioned properties (see Table 1).

In contrast to prior works, UDC seeks to optimize the NN architecture, weight bitwidths, and layer sparsity rates by directly solving a joint search problem over the design choices. Building upon differentiable NAS (DNAS) [43], we exploit efficient weight sharing [48], while addressing key challenges like how to explore the design space while still guaranteeing that the final solution satisfies the constraints. The contributions are further summarized below:

- **Unstructured Pruning & Quantization in DNAS** We extend the DNAS formalism to learn layer-wise weight sparsity levels. We also present a method for searching for sparsity levels in conjunction with layer bitwidths.

<sup>1</sup>Notably, unstructured pruning papers often only report the number of non-zero parameters [25, 37, 42, 58], rather than the true storage cost [14].

- **Highly Diverse Search Spaces in DNAS** Existing DNAS approaches are unable to traverse the exceedingly complex search space required for TinyML (Table 4). We identify desirable DNAS characteristics and propose a novel algorithm to meet these needs.
- **Novel Sparse, Low-Bitwidth Representation** UDC yields compressible models that can be very difficult to train. We identify the root cause of this and propose a solution using a novel weight representation.
- **Extremely Small, SOTA Models** Using UDC, we find compact, compressible NNs Pareto dominant with respect to the state of the art (SOTA) on CIFAR100, ImageNet (Fig. 1), and DIV2K datasets [8, 36, 49].

## 2. Searching for Compressible Models

Compressible models have weights with low entropy. For a given weight tensor  $\theta$ , entropy can be reduced by applying one or more of the following optimizations: 1) make  $\theta$  sparse, 2) quantize  $\theta$ , 3) remove entire channels from  $\theta$ .

**Sparsity** Sparse tensors can be expressed as  $\theta \odot m$ ,  $\|m\|_0 / |m| = s$  where  $m$  is a binary mask,  $\odot$  denotes element-wise multiplication,  $|m|$  is the number of elements in  $m$ , and  $s$  is the percentage of non-zeros. Selecting which elements of  $m$  to set to 0 is a search problem of its own, but we use the popular heuristic of setting the non-zeros to correspond to the  $s \times |m|$  largest magnitude elements of  $\theta$  [27, 30, 42]. Choosing  $s$  is also a hard search problem [22, 23]. As  $s$  decreases, entropy falls, but so does the expressivity of the respective NN layer. We model uncertainty about the best  $s$  to use as a choice amongst  $\{s_1, \dots, s_K\}$ , which can be written as the random variable (RV)

$$m(\pi_s) = \sum_{k=1}^K z_k m_k, \|m_k\|_0 / |m_k| = s_k \quad (1)$$

where  $z = [z_1 \dots z_K] \sim \text{Cat}(\pi_s)$  and  $\text{Cat}(\pi)$  is a categorical distribution parameterized by  $\pi$ . We refer to  $z$  as a decision variable and to  $s_k$  as an option.

**Quantization** Uniformly quantized tensors are given by

$$Q(\theta, b, r) = \begin{cases} d \times \text{round}\left(\frac{\text{clip}(\theta, -r, r)}{d}\right) & b > 1 \\ \text{sign}(\theta) & b = 1 \end{cases} \quad (2)$$

where  $r > 0$  is the quantization range,  $b$  is the bitwidth, and  $d = r / (2^{b-1} - 1)$ . The selection of  $b$  represents a trade-off between compressibility (low  $b$ ) and expressivity (high  $b$ ). We express uncertainty about  $b$  as the RV  $q(\pi_q) = \sum_{k=1}^K z_k Q(\theta, b_k, r_k)$ ,  $z \sim \text{Cat}(\pi_q)$  where each bitwidth  $b_k$  is parameterized by its own range  $r_k$ . For simplicity of notation, we write the summations in both (1) and  $q(\pi_q)$  over  $K$ , but the dimension of  $z$  can vary.

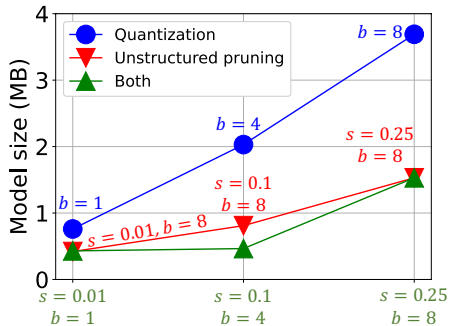


Figure 2. MobileNetV2 compressed for NPU using Vela compiler [3] for different bitwidths,  $b$ , and non-zero ratios per layer,  $s$ .

Sparse, quantized tensors are modeled using  $Q(\theta, b, r) \odot m$ . We found that setting the non-zero values of  $m$  based on  $\theta$  is superior to using  $Q(\theta, b, r)$ , which throws away a significant amount of information about the relative magnitude of weights during the quantization process. To model tensors whose sparsity level and bitwidth are unknown a-priori, we define the RV  $q(\pi_q) \odot m(\pi_s)$ .

**Operator Selection** The compressibility of a NN depends not only on the properties of its weights, but also on the operators used. For example, depthwise separable convolutions require less parameters than regular convolutions, while producing the same number of output feature maps. We frame the uncertainty about operator type as the RV  $\sum_k z_k f_k(x, \theta_k)$  where each operator has a (possibly) different functional form  $f_k(\cdot)$  parameterized by its own weights  $\theta_k$  and  $x$  is the layer input. By including identity as a candidate operation, we can also search over depth.

**Width Selection** Layer widths are central to the NN architecture, and modelled as  $f(x, \theta) \odot w, \|w\|_0 / |w| = \rho$  where  $w$  is a binary mask to toggle any given channel and  $\rho$  is the percentage of non-zero channels. We adopt the convention of setting the first  $\rho\%$  of the channels of  $w$  to 0 [54]. Different choices  $\{\rho_1, \dots, \rho_K\}$  of layer width can be modelled by the RV  $w(\pi_w) = \sum_k z_k w_k, z \sim \text{Cat}(\pi_w)$ .

**Search Space Summary** The UDC search space is visualized in Fig. 3. To maximize weight sharing, the same  $\theta$  is used by the sparsity, bitwidth, and width search modules. The output of a given NN layer can then be expressed as the RV  $(\sum_k f_k(x, q(\pi_q) \odot m(\pi_s))) \odot w(\pi_w)$ .

### 2.1. Measuring Compressibility

In order to optimize for NN compressibility, we need a quantitative measure of it. For any NN layer, the number of bits needed to store its parameters is lower-bounded by its entropy,  $H(\cdot)$ , times the number of elements: (Appendix C)

$$H(Q(\theta, b, r) \odot m) \times \|w\|_0 \leq (b + H(m)) \times \|w\|_0 \quad (3)$$

where  $H(m) = -s \log_2 s - (1-s) \log_2 (1-s)$ . The advantage of the right hand side (RHS) of (3) over the left

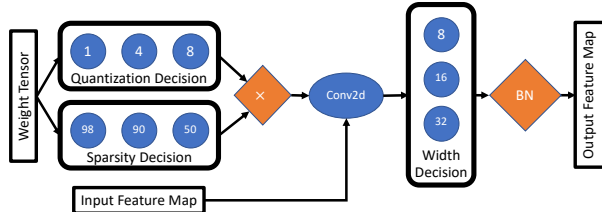


Figure 3. UDC search space overview. BN denotes batch norm.

hand side (LHS) is that it can be computed cheaply without processing  $\theta$ . To compute the LHS, the entropy must be approximated numerically, which requires expensive computation of the statistics of a large tensor. Moreover, gradient approximation is needed to combine the LHS with a gradient-based optimizer, since the numerical entropy is not differentiable [52]. We refer to the RHS of (3) as the compressed tensor size and Section 6.2 confirms that it is achievable with a practical compression algorithm.

Let  $\mathcal{E}(s, b, \rho)$  denote some measure of a given layer’s cost (e.g. size in bits or operation count), as a function of sparsity  $s$ , bitwidth  $b$ , and non-zero channel percentage  $\rho$ . When  $(s, b, \rho)$  is random, we use  $\mathcal{E}(\sum_k z_k s_k, \sum_k z_k b_k, \sum_k z_k \rho_k)$  to measure the layer. For the entire NN, we sum the measure of all individual layers and denote the result  $\mathcal{E}(\{z\})$ , where  $\{z\}$  is short-hand for the set of all decision variables.

## 3. Proposed DNAS Algorithm

DNAS has several advantages compared to black-box methods like Bayesian optimization and evolutionary search. DNAS techniques relax the categorical decision variables, such that optimization can be done using gradient descent. DNAS is parameter efficient because the same underlying weights  $\theta$  are shared, obviating the need to train each possible configuration from scratch. This is in stark contrast to black-box approaches, which require expensive training of many unique NNs from scratch. A number of proxies have been employed in black-box NAS to relax the computational burden, such as training for a short amount of time [21], constraining new evaluations to be morphs of previously evaluated NNs whose weights can be inherited [20], and one-shot approaches [15]. However, the use of proxies assumes a search space where performant models are relatively dense, such that the probability of sampling a performant model from the search space at random is high. Since our search space is more complex than previous work, performant models can be quite rare, as shown in Section 6.1.

Our optimization objective is:

$$\arg \min_{\{\pi, \theta, m, r\}} E_{\{z\}, \mathcal{D}} [L(\{z, \theta\}, \mathcal{D}) \text{ s.t. } \mathcal{E}(\{\gamma(\pi)\}) = e^*, \quad (4)$$

where  $\gamma(\pi) = \text{onehot}(\arg \max_k \pi[k])$ ,  $L(\cdot)$  is a task loss, e.g. cross-entropy for classification problems,  $\mathcal{D}$  is the

training data, and  $e^*$  is the target. We include one efficiency constraint in (4), but we do so only for brevity and without loss of generality. The constraint in (4) is motivated by the two-stage process typically used in DNAS: 1) Solve an optimization problem over  $\{\pi, \theta\}$  and extract the most likely configuration  $\{\gamma(\pi)\}$ , 2) Train and deploy the result [18, 19, 35, 43, 54, 57]. Unlike prior works, which use a constraint of the form [18, 19, 26, 35, 54]

$$E_{\{z\}}[\mathcal{E}(\{z\})] = e^*, \quad (5)$$

we constrain the *most likely* configuration since this is what actually gets deployed. In fact, if (5) is satisfied, there is no guarantee that  $\{\gamma(\pi)\}$  will also satisfy the constraint.

Solving (4) using gradient-based methods like stochastic gradient descent (SGD) requires: 1) ensuring that the constraint is met, 2) computing the derivative of the objective with respect to both  $\{\theta\}$  and  $\{\pi\}$ . Dealing with the constraint raises several issues. Although it may be possible to perform projected gradient descent, where  $\{\pi\}$  is projected onto the constraint manifold after every gradient update, such a scheme would prevent exploration of the search space (Section 3.1) by immediately snapping  $\{\pi\}$  onto one viable, but potentially sub-optimal, solution. Moreover, projecting  $\{\pi\}$  onto the constraint manifold is itself a combinatorial optimization problem. To deal with the exploration issue, we adopt a Lagrangian formulation and to get around the difficulty of dealing with the non-differentiable  $\gamma(\pi)$  directly, we introduce  $\mathcal{L}_{\mathcal{E}}^z$ , modifying (4) to

$$\arg \min_{\{\pi, \theta, m, r\}} \underbrace{E_{\{z\}, \mathcal{D}}[L(\{z, \theta\}, \mathcal{D})]}_{\mathcal{L}_{\text{task}}} + \lambda \underbrace{E_{\{z\}}[\mathcal{E}(\{z\}) - e^*]}_{\mathcal{L}_{\mathcal{E}}^z} \quad (6)$$

While  $\mathcal{L}_{\mathcal{E}}^z$  has a different form than the constraint in (4), it actually represents a much stronger constraint and its minimization implies the constraint is met.

**Lemma 3.1.** *If  $\mathcal{L}_{\mathcal{E}}^z = 0$ , then for any sample of  $\{z\}$ , denoted  $\{z^s\}$ , with non-zero probability,  $\mathcal{E}(\{z^s\}) = e^*$  and  $\mathcal{E}(\{\gamma(\pi)\}) = e^*$ .*

$\mathcal{L}_{\mathcal{E}}^z$  differs from (5) because it penalizes any configuration which violates the constraint, whereas (5) penalizes  $\{\pi\}$  only if the expected efficiency violates the constraint.

Turning to 2, the derivative of (6) with respect to  $\{\theta\}$  can be approximated by using a Monte-Carlo (MC) approximation of the expectation and applying any standard automatic differentiation tool to the result. The derivative with respect to  $\{\pi\}$  is more complex since the expectations in (6) depend on  $\{\pi\}$ . The most popular solution in the DNAS literature [18, 19] is to use a biased but differentiable approximation of  $z$ , given by the Gumbel-softmax distribution [34]:

$$\hat{z} = \text{softmax}\left(\frac{\log \pi + g}{\tau}\right), g[k] \sim \text{Gumbel}(0, 1) \quad (7)$$

where  $\tau > 0$  is the temperature. As  $\tau \rightarrow 0$ ,  $\hat{z}$  approaches  $z$  in distribution, while the variance of any gradient estimator which uses  $\hat{z}$  increases ([47] and Fig. 7b). In other

Table 2. Values of  $\mathcal{L}_{\mathcal{E}}^z$  for different values of  $\tau$  and  $\vartheta$ . The search space is based on MobileNetV2 (Section 6) and the model size is constrained to  $e^* = 0.5$ . In all cases,  $\mathcal{E}(\{\gamma(\pi)\}) = e^*$ .

	$\xi^t = 1, \vartheta = 0$	$\xi^t = 0.5, \vartheta = 0$	$\xi^t = 0.5, \vartheta = 0.5$	$\xi^t = 0.5, \vartheta = 0.99$
$\tau$	10	0.53	0.61	0.6
	0.66	0.04	0.33	0.27
				0.59
				0.18

words, as the bias of the gradient estimator is reduced, its variance increases. As a result, the common practice is to anneal  $\tau$  from a high value to a low one throughout training. In practice, we observe two issues with annealing  $\tau$ : 1) the increased gradient variance at low  $\tau$ , coupled with our complex search space, causes issues for SGD, 2) when we replace  $z$  with  $\hat{z}$  in  $\mathcal{L}_{\mathcal{E}}^z$ , denoting the result  $\mathcal{L}_{\mathcal{E}}^{\hat{z}}$ , the constraint takes on a different meaning. To understand the impact of  $\tau$  on  $\mathcal{L}_{\mathcal{E}}^z$ , we evaluate  $\mathcal{L}_{\mathcal{E}}^z$  for different values of  $\tau$ , setting  $\pi$  such that  $\{\gamma(\pi)\} = e^*$ . The results are presented in Table 2, column 1 and show that increasing  $\tau$  increases  $\mathcal{L}_{\mathcal{E}}^z$ . Therefore, the relative impact of  $\mathcal{L}_{\mathcal{E}}^z$  on (6) depends on  $\tau$ .

As such, we seek to keep  $\tau$  as low as possible, while keeping gradient variance under control. One solution is to use multiple samples of  $\{\hat{z}\}$  in the MC approximation of (6). To maintain the same computational cost as the single MC sample case, we divide the number of optimization steps by the number of MC samples. This approach is identical to that of data-parallel multi-GPU training, where total batch size is increased linearly with the number of GPUs. In addition to reducing gradient variance, our multi-MC-sample strategy has two additional practical benefits: 1) extension a multi-GPU system is trivial since each GPU can run its own MC sample and gradient computation, 2) the overheads associated with computing the gradient are amortized across the number of MC samples. We observe a significant speed-up when going from 1 MC sample to 32 per gradient update, as shown in Table 4, column 6.

While samples of  $z$  are one-hot, samples of  $\hat{z}$  are not. This property can cause issues for an approach like DNAS, where weight-sharing can lead to co-adaptation between search options [28, 32]. The result is a large performance drop when finetuning  $\{\gamma(\pi)\}$ , compared to the value of  $\mathcal{L}_{\text{task}}$  achieved by solving (6) [33]. One solution, which we adopt, is to use a straight-through-estimator (STE), whereby

$$\hat{z}_f[k] = \begin{cases} \hat{z}[k] / \|\hat{z}_f\|_1 & k \in \text{topk}(\hat{z}, \kappa) \\ 0 & \text{else} \end{cases} \quad (8)$$

is used in the forward pass, where  $\kappa$  is the number of non-zeros in  $\hat{z}_f[k]$ ,  $\text{topk}(\hat{z}, \kappa)$  returns the indices of the  $\kappa$  largest elements of  $\hat{z}$ , and  $\hat{z}$  is used in the backward pass [34].

### 3.1. Exploration-Exploitation

In the context of solving (6) with a fixed computational budget of  $B$  SGD steps, we can define exploration/exploitation explicitly. Maximal exploration means

optimizing every possible configuration  $\{z\}$  and its associated weights for  $B/K^D$  SGD steps, where  $D$  denotes the number of decisions and we assume, for ease of exposition, that all decisions have  $K$  options. Maximal exploitation means optimizing a single configuration and its associated weights for  $B$  SGD steps. The goal is to balance exploration and exploitation, giving as many configurations as possible a chance to be trained while still training the explored configurations for a meaningful number of steps.

We propose to explicitly control the exploration-exploitation trade-off by projecting  $\pi$  onto the set  $\mathcal{S} = \{\pi : \max_k \pi[k] \leq 1/K + \xi^t\}$  after each SGD step, where  $\xi^t$  is the upperbound on  $\pi$  at step  $t$ . Setting  $\xi^t = 0$  constrains  $\pi$  to a uniform distribution and represents maximal exploration. On the other hand,  $\xi^t = 1 - 1/K$  removes the constraint on  $\pi$ , allowing the optimizer to enter full exploitation (Section 3.3). To project  $\pi$  onto  $\mathcal{S}$ , we could define a distance metric and minimize the distance between  $\pi$  and the closest point to  $\pi$  in  $\mathcal{S}$ . Instead, we define the projection operator directly, keeping the distance metric implicit, because our goal is to keep the relative ordering of options by likelihood between  $\pi$  and  $P_{\mathcal{S}}(\pi)$ , the projection of  $\pi$  onto  $\mathcal{S}$ , the same: if  $\pi[k] < \pi[k']$ , then  $P_{\mathcal{S}}(\pi)[k] < P_{\mathcal{S}}(\pi)[k']$ . We define  $P_{\mathcal{S}}(\pi) = \text{softmax}(\log \pi / T^*)$ ,  $T^* = \arg \min_T \sum_k \max(P_{\mathcal{S}}(\pi)[k] - \xi^t, 0)$ , which we solve numerically, initialized with  $T = 1$ .

### 3.2. Rejection Sampling

Bounding  $\pi$  to reside on  $\mathcal{S}$  enables explicit control over the algorithm’s exploration-exploitation dynamics, but it also inflates  $\mathcal{L}_{\mathcal{E}}^{\hat{z}}$ . Table 2, column 2 shows the effect of setting  $\xi^t = 0.5$  on  $\mathcal{L}_{\mathcal{E}}^{\hat{z}}$ :  $\mathcal{L}_{\mathcal{E}}^{\hat{z}}$  increases dramatically, especially at low  $\tau$ . By forcing  $\pi$  to be closer to uniform, the number of configurations  $\{\hat{z}\}$  with non-zero probability increases, such that the probability of a randomly drawn configuration violating the efficiency constraint also increases. Such behavior is undesirable, since inflating  $\mathcal{L}_{\mathcal{E}}^{\hat{z}}$  forces the optimizer to focus less on  $\mathcal{L}_{\text{task}}$ , leading to solutions which meet the constraint but perform poorly on the target task.

$\mathcal{L}_{\mathcal{E}}^{\hat{z}}$  increases when the properties of  $\{\pi\}$  change because it depends on all possible configurations  $\{\hat{z}\}$  instead of the most likely one, i.e.  $\{\gamma(\pi)\}$ . To motivate the remedy, we first observe that while not all samples of  $\hat{z}$ , denoted  $\hat{z}^s$ , satisfy  $\gamma(\hat{z}^s) = \gamma(\pi)$ , some do. Indeed,  $\mathcal{L}_{\mathcal{E}}^{\hat{z}}$  would be 0 if it was only evaluated over those samples that satisfy  $\gamma(\hat{z}^s) = \gamma(\pi)$ , assuming  $\kappa = 1$  for the STE in (8) and  $\mathcal{E}(\{\gamma(\pi)\}) = e^*$ . We refer to samples generated in this manner as  $\tilde{z}^s$  and they correspond to a random variable  $\tilde{z}$  whose distribution is different from  $\hat{z}$ , but still depends on  $\pi$  and can therefore be used to generate gradients to  $\pi$  from  $\mathcal{L}_{\mathcal{E}}^{\tilde{z}}$ . Alg. 1 outlines the process of generating realizations of  $\tilde{z}$ . Replacing  $\hat{z}$  with  $\tilde{z}$  for all decisions negates the effects of controlling  $\pi$  through projection onto  $\mathcal{S}$ . Therefore, we use  $\tilde{z}$  for a given decision

with probability  $\vartheta$  and use  $\hat{z}$  otherwise.

---

#### Algorithm 1 Rejection sampling algorithm

---

- 1: Sample  $\hat{z}^s \sim p(\hat{z})$ ,  $1 \leq s \leq S$
  - 2:  $\tilde{s} = 1$ ,  $k^* = \arg \max_k \pi[k]$
  - 3: **for**  $1 \leq s \leq S$  **do**
  - 4:      $\hat{k} = \arg \max_k \hat{z}^s[k]$
  - 5:     **if**  $\hat{k} = k^*$  **then**
  - 6:          $\tilde{z}^{\tilde{s}} = \hat{z}^s$ ,  $\tilde{s} = \tilde{s} + 1$
  - 7:  $\tilde{z} = \frac{1}{\tilde{s}-1} \sum_{s'=1}^{\tilde{s}-1} \tilde{z}^{s'}$  ▷ Average
  - 8: **return**  $\tilde{z}$
- 

---

#### Algorithm 2 Complete UDC algorithm

---

- 1: **for**  $1 \leq t \leq t_{\max}$  **do**
  - 2:     **for**  $1 \leq s \leq S$  **do**
  - 3:         Generate MC sample  $s$  for decision  $j$  using  $\hat{z}_j$   
w.p.  $\vartheta$  and  $\tilde{z}_j$  else ▷ Sample
  - 4:         Apply (8) to  $\hat{z}_j^s$  or  $\tilde{z}_j^{s'}$  ▷ STE
  - 5:         Update  $\{m\}$  if  $t$  modulo 16 = 0
  - 6:         Take SGD step on (6)
  - 7:          $\pi \leftarrow P_{\mathcal{S}}(\pi)$  ▷ Projection
  - 8: **return**  $\{\pi\}$
- 

Using  $\tilde{z}$  has two major benefits. First, even when exploration is actively being enforced by projecting  $\pi$  onto  $\mathcal{S}$ ,  $\mathcal{L}_{\mathcal{E}}^{\tilde{z}}$  does not get inflated. Table 2, columns 3-4 show how  $\vartheta > 0$  brings down  $\mathcal{L}_{\mathcal{E}}^{\tilde{z}}$  for the same underlying  $\{\pi\}$ . Second, mixing  $\hat{z}$  and  $\tilde{z}$  gives the flexibility of being in exploration for some decisions and exploitation for others, respectively. By randomly choosing which decisions use  $\hat{z}$  and which use  $\tilde{z}$ , we prevent greedy behavior whereby a given decision enters exploitation and never returns to exploration.

### 3.3. Implicit Exploitation Through Regularization

While we find it necessary to enforce exploration by projecting  $\pi$  onto  $\mathcal{S}$ ,  $\mathcal{L}_{\mathcal{E}}^{\tilde{z}}$  implicitly promotes exploitation.

**Lemma 3.2.** *Let  $\mathcal{L}_{\mathcal{E}}(\{z\}) = 0$  and  $z_j$  be the  $j$ ’th decision variable. Let there be no decision for which two of its options have the same cost, i.e. for two configurations  $\{z^s\}$  and  $\{z^{s'}\}$  such that  $z_j^s \neq z_j^{s'}$  and  $z_k^s = z_k^{s'} \forall k \neq j$ , we have  $\mathcal{L}_{\mathcal{E}}(\{z^s\}) \neq \mathcal{L}_{\mathcal{E}}(\{z^{s'}\})$ . Then each  $\pi_j$  must be one-hot.*

The assumption in Lemma 3.2 that no decision has two options with the same cost is satisfied for the model size constraint with a typical compressible model search space.

The complete UDC algorithm is summarized in Alg. 2.

## 4. Training Sparse, Quantized Models

DNAS is typically a two-stage process; a search phase to find a viable NN architecture is followed by a finetuning

Table 3. NN weight norm following training with various settings.

	After stage 1	After stage 3 w/ baseline representation	After stage 3 w/ proposed representation
$\ \theta\ _2^2$	1.7e3	7.9e3	3.7e3

phase to find optimal weights for the architecture. However, we find that the second stage yields poor results when training sparse, quantized models from scratch [63].

Instead, UDC employs a three-stage finetuning process: 1) initialize NN weights randomly and train with quantization enabled but unstructured pruning disabled, 2) enable unstructured pruning gradually, and 3) train with both quantization and unstructured pruning fully enabled.

To counter the noise introduced by quantizing and pruning  $\theta$ , we employ several techniques from the model compression literature, with one slight modification. For quantization, we use a variant of [51] where each NN weight is quantized with probability  $\alpha$  during a given forward pass, such that the weights used for training are  $Q(\theta, b, r) \odot g + \text{clip}(\theta, -r, r) \odot (1 - g)$  where  $g$  is a binary mask with elements following Bernoulli( $\alpha$ ). Unlike UDC, [51] uses  $\theta$  directly in the second term. We observe that the dynamic range of  $\theta$  can differ significantly from that of  $Q(\theta, b, r)$ , especially when unstructured pruning is applied during the learning process, so we clip  $\theta$  to the same range as  $Q(\theta, b, r)$ . To counter noise induced by unstructured pruning, we gradually anneal the pruning rate from 0% to 100% of the target rate during training [42, 64].

**Weight Numerical Representation** To gain intuition about the challenge of training sparse, quantized NNs, consider a single layer of pretrained weights, with histogram in Fig. 4a. The quantization bins ( $b = 4$ ) are shown as red lines and the pruning boundary as green lines, with everything between the green lines mapped to 0. The sparse quantization problem is clearly apparent here: 8/14 of the non-zero quantization bins are unused because they fall inside the pruning boundary. If we now train the NN, with weight sparsity and bitwidth constraints, the weight distribution, quantization bins, and pruning zone adjust (Fig. 4b). The optimizer flattens the weight distribution to try to use more quantization bins, resulting in increased range. To quantify the weight growth, we report the  $\ell_2$  norm of the NN weights after stage 1 (Table 3, col. 1) and after stage 3 (Table 3 col. 2), showing a dramatic increase of over  $4.6\times$ . Although NNs with batch normalization are invariant to weight norm, the rate at which NNs can be trained, known as the effective learning rate, is inversely proportional to the weight norm [10]. Therefore, the interaction of sparsity and quantization cause weight norm inflation, which decreases the effective learning rate, reducing NN performance.

To address this challenge of training sparse, quantized NNs, we propose a different weight representation. Our

approach is to only quantize the range beyond the pruning boundary (Fig. 4c), using a modified quantization operator

$$Q(\theta, b, r, \beta) = Q(\theta - \text{sign}(\theta)\beta, b, r) + \text{sign}(\theta)\beta \quad (9)$$

for  $b > 1$ , where  $\beta \in \mathbb{R}$ . In practice, we set  $\beta$  to be the largest pruned value of  $\theta$ , but  $\beta$  can also be learned via SGD.

**Deployment with Integer Math** NPU and MCU HW platforms typically only support integer operations, which are much cheaper than floating point. There are at least two ways of deploying NNs quantized using (9) on such HW. Firstly, any linear operation like convolution can be decomposed into  $f(x, Q(\theta - \text{sign}(\theta)\beta, b, r)) + \beta f(x, \text{sign}(\theta))$ . Both terms can be calculated using only integer math, but since  $\text{sign}(\theta)$  is a 1-bit tensor, it does not require any multiplications and is very cheap. Secondly, the NN can be trained using (9), then deployed with  $Q(Q(\theta, b, r, \beta), b^*, r')$ , such that the deployed NN is quantized using uniform quantization, with  $b^* = 8$  to match the common datatype supported in MCUs/NPUs [2, 5, 6]. The advantage of approach two is that NN training benefits from the expressivity of (9), while its deployment uses a standard data type. We find that approach two with  $b^* = 8$  does not incur an accuracy loss on ImageNet (Fig. 1).

## 5. Related Work

Table 1 contrasts UDC with the most relevant previous work. MCUNet [41] is the closest work to UDC in terms of designing accurate NNs for large scale datasets like ImageNet while targeting the TinyML HW form-factor with severely limited memory. However, UDC is fundamentally different to MCUNet: 1) unlike MCUNet, UDC also performs a search of bitwidths and sparsity rates to exploit HW compression, 2) UDC is a DNAS algorithm whereas MCUNet uses evolutionary search of a pre-trained once-for-all (OFA) [15] supernet. In particular, the UDC search space targets compressible models and is much more diverse than that of MCUNet; training a single OFA supernet for our search space would be infeasible.

In common with UDC, two previous works have considered network optimizations [56, 58]. Yang *et al.* demonstrate learning layer bitwidths and sparsity rates [58], but differ significantly from UDC in that they: 1) do not consider the cost of storing the pruning mask  $m$ , often a significant portion of the model size at high sparsity [14], which would inflate the reported model size for practical deployment; 2) only consider optimizations, without accompanying network width, depth, or operator search; 3) employ floating-point non-uniform quantization, not deployable on TinyML MCU and NPU platforms which only support integer operations. Wang *et al.* propose a multi-stage algorithm to search over layer width and bitwidth [56]. Compared to [56]: 1) UDC optimizes over sparsity rates whereas [56] does not, which is essential to achieve compressible models

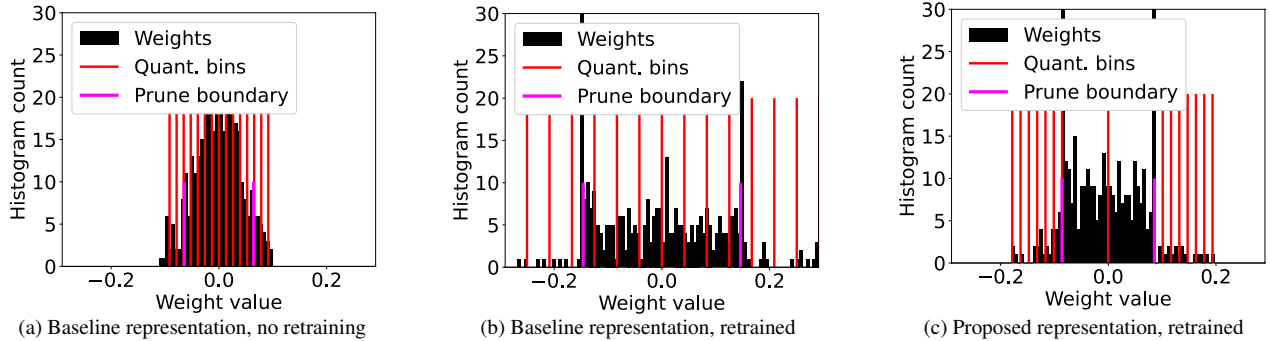


Figure 4. Histogram of weights from a single pruned and quantized layer in the ImageNet experiment under different conditions.

for NPUs deployment; 2) [56] does not report actual model sizes, so it is unfortunately difficult to compare on this basis. Finally, other relevant works include Gong *et al.* [26], which searches over width and bitwidth but not sparsity, Choi *et al.* [17], which searches over bitwidth and sparsity but not layer widths and without constrained optimization, and Uhllich *et al.* [53] which searches over only bitwidths.

## 6. Results

We compare UDC with SOTA methods on a model size versus accuracy basis. All reported model sizes, including related works, use compressed size (RHS of (3)), except Choi *et al.* [17], who use bzip2 to compress weights and we use their reported sizes.

**CIFAR100** An image recognition dataset with 50k training / 10k test images, and 100 classes. Our search space is based on the wide residual architecture with depth 20 and width multiplier 10 [44, 62]. We search over layer width (increments of 10% of the original), bitwidth (1, 2, 4, 8, 32), and sparsity (1 – 100% non-zeros, increments of 10%). We use UDC with the settings described in Appendix D to find and train models at two sizes: 0.55MB and 0.7MB. Fig. 5a compares our results with SOTA methods [26, 44] to demonstrate that UDC can generate Pareto-dominant NNs.

**ImageNet** An image recognition dataset with 1.28e6 training / 50k test images, and 1k classes. Our search space is based on MobilenetV2 [50], searching over the same options as the CIFAR100 experiment, and targeting models at size constraints of 0.5, 1, and 1.25 MB (Appendix E). For the 1.25MB experiment, we replace 3×3 kernels with 5×5 and make all layers 1.5× wider in the baseline architecture. The search takes ~ 5.4 days on 2 Nvidia Quadro RTX 8000 GPUs. Fig. 1 shows that UDC generates pareto-dominant NNs with respect to the SOTA [17, 26, 40, 41].

Next, we include depth/operators in the search space, considering two alternatives to the inverted bottleneck: 1) regular 3×3 convolution, 2) identity. We target a 0.5MB model size with the same backbone as used for the 0.5MB ImageNet experiment above. Interestingly, UDC chooses inverted bottleneck blocks everywhere, such that the model

found by including depth/operators in the search is identical to the one found when depth/operators are excluded.

In addition, we compare UDC to approaches which employ non-uniform quantization in Appendix G. The results indicate that UDC generates pareto-dominant models even though approaches like [55, 58] employ a more expressive, non-uniform type of quantization which cannot be deployed on commodity MCUs and NPUs running integer math operations. We also compare UDC to a SOTA unstructured pruning algorithm in Fig. 9, which shows that UDC finds considerably more accurate models.

**Super Resolution** The purpose of the super resolution experiment is two-fold: 1) show that UDC can be applied to regression problems as well as classification, 2) demonstrate UDC in a setup which constrains the computational complexity of the NN, measured in number of multiply-and-accumulate (MAC) operations, instead of size. The experiment uses the search space in Section 2, excluding bitwidth and sparsity, which do not impact the inference compute cost. The topology of our search space is inspired by FSRCNN, with search over model depth, width, and kernel size. We use div2k dataset with 2x upscaling and report MACs for a input patch of 64x64. We train all networks, including those from [13], using the same settings. Fig. 5b shows that UDC generates Pareto-dominant NNs compared with a SOTA efficient super resolution method [13].

### 6.1. Comparison with Random Search

Simple random search methods [39] can actually compete with DNAS in some settings. As such, random search with early stopping [39] is a strong baseline. However, we train sparse networks in stages, with sparsity only applied during stages 2-3, which is too late in the process to save time from stopping. Fig. 6a compares UDC to randomly generated NNs constrained to model sizes < 0.55MB for CIFAR100, with the search space used in Fig. 5a. Results show that NNs in our search space which satisfy the size constraint and achieve high accuracy are rare. The gap between the best models found by UDC and random search is a significant 4.77%. Fig 6b shows the best accuracy achieved by random search after a given number of trials.

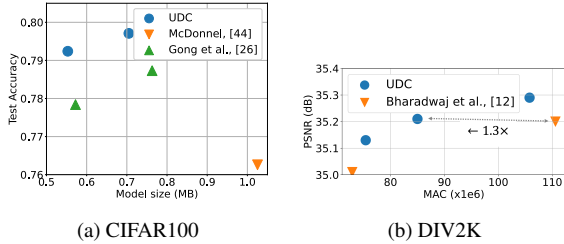


Figure 5. UDC finds pareto-dominant models on image tasks.

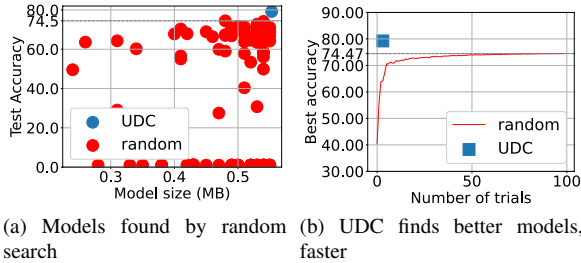


Figure 6. Comparison of UDC with random search.

To integrate out the randomness induced by the ordering of the trials, we permute the order of the random search results 100× and average over all of the permutations. Since we observe that UDC NAS requires  $\sim 2\times$  longer to find a NN than training a baseline NN, we plot the cost of UDC as 3 trials (2 to search and 1 to train the resulting NN) in Fig. 6a. These results confirm that UDC finds better NNs and is significantly more efficient than random search.

## 6.2. Ablations

All reported model sizes are computed using the RHS of (3) assuming that the pruning mask  $m$  can be compressed close to the entropy limit. To verify this, we compressed  $m$  using arithmetic coding [45] for all UDC models in Fig. 1, observing that theoretical and practical compressed model sizes are within two decimal places.

We also compared our reported model sizes to those produced by the Vela compiler for Arm Ethos-U55 NPU. For UDC models targeting 0.5, 1, and 1.25MB, Vela reports model sizes: 0.17, 0.2, and 0.4MB larger, respectively. This gap is due to the meta-data which describes the NN itself [12]. The meta-data size is dependent on the NN, which is why the larger model saw largest compiled overhead<sup>2</sup>.

To measure the impact of the individual components in Section 3, we conduct an ablation using the CIFAR100 search space above (Table 4). In addition to final task accuracy, we also evaluate methods based on whether or not they require a hyperparameter search over  $\lambda$  and their runtime in GPU days (GPUD). Rows 3 and 4 show that disabling either

<sup>2</sup>Although Vela does not report the meta-data size, it can be estimated by compressing models with all weights set to 0, which are then heavily compressed until negligible, leaving meta-data only. Accounting for the meta-data, Vela compresses model weights to 0.3, 0.71, and 0.94MB.

Table 4. Ablation on UDC components. \*—Constraint not met. †—GPUD excludes hyperparameter search for  $\lambda$ . Fifth row: constraint grossly violated even after tuning  $\lambda$ , so accuracy not reported.

Rejection Sampling	Multiple MC Samples	$\pi$ Projection	No $\lambda$ Tuning	Acc	GPUD
✓	✓	✓	✓	79.24	1.17
✓	✓	✗	✗	76.48	0.75 <sup>†</sup>
✗	✓	✓	✓	79.14	1.17
✗	✗	✓	✓	79.06	6.21
✗	✓	✗	✓	*	0.83
✗	✓	✗	✗	75.25*	1.58 <sup>†</sup>
✗	✗	✗	✗	77.89*	6.21 <sup>†</sup>

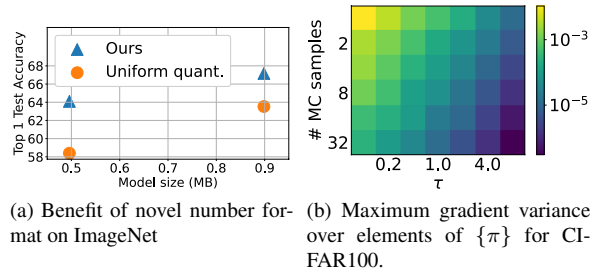


Figure 7. Ablations

rejection sampling or multiple MC samples hurts the model quality slightly, but not significantly and the search is still able to find NNs that meet the constraint without needing to tune  $\lambda$ . Row 2 shows that disabling  $\pi$  projection produces much worse models and requires tuning  $\lambda$ . The last three rows show that disabling projection of  $\pi$  on  $\mathcal{S}$  in conjunction with disabling either rejection sampling or multiple MC samples results in missing the efficiency constraint even with  $\lambda$  tuning. Moreover, the discovered NNs are up to 4% less accurate than the NN found by UDC. The last row represents the basic DNAS algorithm reported in the literature [18], with the exception that the regularizer in (4) is used instead of (5), which finds a NN that is 1.35% worse than UDC while still not meeting the constraint.

Fig. 7a shows the benefit of the proposed number format in isolation by training two UDC networks and comparing with the baseline number format in (2).

## 7. Societal Impact & Limitations

The development of UDC consumed hundreds of energy-consuming GPU hours. However, this development cost can actually be amortized if it is used to deploy efficient models across billions of IoT devices. One limitation of UDC is that we retrain  $\{\theta\}$  for every constraint  $e^*$ , whereas approaches based on OFA can amortize the cost of training  $\{\theta\}$  across multiple constraints.

## 8. Conclusion

Emerging NPU HW platforms specialized for TinyML support model compression, whereby quantized and pruned NNs can be stored in a reduced memory footprint. While compression is highly desirable, it increases the complexity of the NN design process, as the space of candidate NNs is



increased by adding quantization and pruning on top of the conventional NN architecture choices. To enable TinyML practitioners to fully exploit HW model compression in NPUs, we describe a unified DNAS framework to search both architecture choices and aggressive per-layer quantization and pruning. We describe a number of improvements on top of DNAS, allowing us to demonstrate SOTA TinyML models that fully exploit model compression, as well as a comparison with random sampling and extensive ablations. UDC finds NNs  $1.35\times$  smaller than MCUNet and 2.26% more accurate than MCUNetV2 on ImageNet.

## References

- [1] Alif Semiconductor: Introducing the Ensemble and Crescendo families of fusion processors and microcontrollers. <https://alifsemi.com/products/>. Accessed: 2019-05-02. **1**
- [2] Arm Ethos-U55 Micro Neural Processing Unit (uNPU). <https://www.arm.com/products/silicon-ip-cpu/ethos/ethos-u55>. Accessed: 2021-10-26. **1, 2, 6**
- [3] Arm Vela Tool for Ethos-U Micro Neural Processing Unit (uNPU). <https://pypi.org/project/ethos-u-vela/>. Accessed: 2021-10-26. **1, 2, 3**
- [4] Practical application of tinyML in battery powered anomaly sensors for predictive maintenance of industrial assets. [https://cms.tinyml.org/wp-content/uploads/talks2020/tinyML\\_Talks\\_Mark\\_Stubbs\\_200818.pdf](https://cms.tinyml.org/wp-content/uploads/talks2020/tinyML_Talks_Mark_Stubbs_200818.pdf). Accessed: 2021-10-09. **1**
- [5] TensorFlow Lite for Microcontrollers. <https://github.com/tensorflow/tensorflow/tree/master/tensorflow/lite/experimental/micro>. Accessed: 2019-05-02. **1, 6**
- [6] uTensor. <http://utensor.ai/>. Accessed: 2019-05-02. **1, 6**
- [7] Visual Wake Words Challenge, CVPR 2019. Accessed: 2019-05-02. **1**
- [8] Eirikur Agustsson and Radu Timofte. Ntire 2017 challenge on single image super-resolution: Dataset and study. In *IEEE/CVF CVPR workshops*, pages 126–135, 2017. **2**
- [9] Hazaar Ahmad, Tabasher Arif, Muhammad Abdullah Hanif, Rehan Hafiz, and Muhammad Shafique. Superslash: A unified design space exploration and model compression methodology for design of deep learning accelerators with reduced off-chip memory access volume. *IEEE Transactions on Computer-Aided Design of Integrated Circuits and Systems*, 39(11):4191–4204, 2020. **1**
- [10] Sanjeev Arora, Zhiyuan Li, and Kaifeng Lyu. Theoretical analysis of auto rate-tuning by batch normalization. In *International Conference on Learning Representations*, 2019. **6**
- [11] Colby Banbury, Vijay Janapa Reddi, Peter Torelli, Nat Jeffries, Csaba Kiraly, Jeremy Holleman, Pietro Montino, David Kanter, Pete Warden, Danilo Pau, Urmish Thakker, antonio torrini, jay cordaro, Giuseppe Di Guglielmo, Javier Duarte, Honson Tran, Nhan Tran, niu wenxu, and xuesong. MLPerf tiny benchmark. In *Thirty-fifth Conference on Neural Information Processing Systems Datasets and Benchmarks Track (Round 1)*, 2021. **1**
- [12] Colby Banbury, Chuteng Zhou, Igor Fedorov, Ramon Matas, Urmish Thakker, Dibakar Gope, Vijay Janapa Reddi, Matthew Mattina, and Paul Whatmough. Micronets: Neural network architectures for deploying tinyml applications on commodity microcontrollers. *Proceedings of Machine Learning and Systems*, 3, 2021. **1, 2, 8**
- [13] Kartikeya Bhardwaj, Milos Milosavljevic, Liam O’Neil, Dibakar Gope, Ramon Matas, Alex Chalfin, Naveen Suda, Lingchuan Meng, and Danny Loh. Collapsible linear blocks for super-efficient super resolution. *arXiv preprint arXiv:2103.09404*, 2021. **7**
- [14] Davis Blalock, Jose Javier Gonzalez Ortiz, Jonathan Frankle, and John Gutttag. What is the state of neural network pruning? In I. Dhillon, D. Papailiopoulos, and V. Sze, editors, *Proceedings of Machine Learning and Systems*, volume 2, pages 129–146, 2020. **2, 6**
- [15] Han Cai, Chuang Gan, Tianzhe Wang, Zhekai Zhang, and Song Han. Once-for-all: Train one network and specialize it for efficient deployment. In *International Conference on Learning Representations*, 2020. **3, 6**
- [16] Han Cai, Ligeng Zhu, and Song Han. ProxylessNAS: Direct neural architecture search on target task and hardware. In *International Conference on Learning Representations*, 2019. **2**
- [17] Yoojin Choi, Mostafa El-Khamy, and Jungwon Lee. Learning sparse low-precision neural networks with learnable regularization. *IEEE Access*, 2020. **1, 2, 7**
- [18] Xuanyi Dong and Yi Yang. Network pruning via transformable architecture search. In *Advances in Neural Information Processing Systems*, pages 759–770, 2019. **2, 4, 8**
- [19] Xuanyi Dong and Yi Yang. Searching for a robust neural architecture in four gpu hours. In *IEEE/CVF CVPR*, pages 1761–1770, 2019. **4, 12**
- [20] Thomas Elsken, Jan Hendrik Metzen, and Frank Hutter. Efficient multi-objective neural architecture search via Lamarckian evolution. In *International Conference on Learning Representations*, 2019. **3**
- [21] Thomas Elsken, Jan Hendrik Metzen, and Frank Hutter. Neural architecture search: A survey. *Journal of Machine Learning Research*, 20(55):1–21, 2019. **2, 3**
- [22] Utku Evci, Trevor Gale, Jacob Menick, Pablo Samuel Castro, and Erich Elsen. Rigging the lottery: Making all tickets winners. In Hal Daumé III and Aarti Singh, editors, *Proceedings of the 37th International Conference on Machine Learning*, volume 119 of *Proceedings of Machine Learning Research*, pages 2943–2952. PMLR, 13–18 Jul 2020. **2**
- [23] Igor Fedorov, Ryan P Adams, Matthew Mattina, and Paul N Whatmough. Sparse: Sparse architecture search for cnns on resource-constrained microcontrollers. *Advances in Neural Information Processing Systems*, 32, 2019. **1, 2**
- [24] Igor Fedorov, Marko Stamenovic, Carl Jensen, Li-Chia Yang, Ari Mandell, Yiming Gan, Matthew Mattina, and Paul N Whatmough. Tinylstms: Efficient neural speech enhancement for hearing aids. *INTERSPEECH*, 2020. **1, 2**

- [25] Trevor Gale, Erich Elsen, and Sara Hooker. The state of sparsity in deep neural networks. *CoRR*, abs/1902.09574, 2019. [2](#)
- [26] Chengyue Gong, Zixuan Jiang, Dilin Wang, Yibo Lin, Qiang Liu, and David Z Pan. Mixed precision neural architecture search for energy efficient deep learning. In *2019 IEEE/ACM International Conference on Computer-Aided Design (ICCAD)*, pages 1–7. IEEE, 2019. [1](#), [4](#), [7](#)
- [27] Yiwen Guo, Anbang Yao, and Yurong Chen. Dynamic network surgery for efficient dnns. In *Proceedings of the 30th International Conference on Neural Information Processing Systems*, pages 1387–1395, 2016. [2](#)
- [28] Zichao Guo, Xiangyu Zhang, Haoyuan Mu, Wen Heng, Zechun Liu, Yichen Wei, and Jian Sun. Single path one-shot neural architecture search with uniform sampling. In *European Conference on Computer Vision*, pages 544–560. Springer, 2020. [4](#)
- [29] Song Han, Huizi Mao, and William J Dally. Deep compression: Compressing deep neural networks with pruning, trained quantization and huffman coding. *International Conference on Learning Representations (ICLR)*, 2016. [2](#)
- [30] Song Han, Jeff Pool, John Tran, and William Dally. Learning both weights and connections for efficient neural network. *Advances in Neural Information Processing Systems*, 28, 2015. [1](#), [2](#)
- [31] Yihui He, Xiangyu Zhang, and Jian Sun. Channel pruning for accelerating very deep neural networks. In *Proceedings of the IEEE International Conference on Computer Vision*, pages 1389–1397, 2017. [2](#)
- [32] Weijun Hong, Guilin Li, Weinan Zhang, Ruiming Tang, Yunhe Wang, Zhenguo Li, and Yong Yu. Dropnas: Grouped operation dropout for differentiable architecture search. In *IJCAI*, pages 2326–2332, 2020. [4](#)
- [33] Shoukang Hu, Sirui Xie, Hehui Zheng, Chunxiao Liu, Jianping Shi, Xunying Liu, and Dahua Lin. Dsnas: Direct neural architecture search without parameter retraining. In *IEEE/CVF CVPR*, pages 12084–12092, 2020. [4](#)
- [34] Eric Jang, Shixiang Gu, and Ben Poole. Categorical reparameterization with gumbel-softmax. *International Conference on Learning Representations*, 2017. [4](#)
- [35] Xiaojie Jin, Jiang Wang, Joshua Slocum, Ming-Hsuan Yang, Shengyang Dai, Shuicheng Yan, and Jiashi Feng. Rc-darts: Resource constrained differentiable architecture search. *arXiv preprint arXiv:1912.12814*, 2019. [4](#)
- [36] Alex Krizhevsky, Geoffrey Hinton, et al. Learning multiple layers of features from tiny images. 2009. [2](#)
- [37] Aditya Kusupati, Vivek Ramanujan, Raghav Somani, Mitchell Wortsman, Prateek Jain, Sham Kakade, and Ali Farhadi. Soft threshold weight reparameterization for learnable sparsity. In *International Conference on Machine Learning*, pages 5544–5555. PMLR, 2020. [2](#), [13](#)
- [38] Haitong Li, Mudit Bhargav, Paul N Whatmough, and H-S Philip Wong. On-chip memory technology design space explorations for mobile deep neural network accelerators. In *2019 56th ACM/IEEE design automation conference (DAC)*, pages 1–6. IEEE, 2019. [1](#)
- [39] Liam Li and Ameet Talwalkar. Random search and reproducibility for neural architecture search. In *Uncertainty in artificial intelligence*, pages 367–377. PMLR, 2020. [7](#)
- [40] Ji Lin, Wei-Ming Chen, Han Cai, Chuang Gan, and Song Han. Mxnetv2: Memory-efficient patch-based inference for tiny deep learning. *arXiv preprint arXiv:2110.15352*, 2021. [7](#)
- [41] Ji Lin, Wei-Ming Chen, Yujun Lin, Chuang Gan, Song Han, et al. Mxnet: Tiny deep learning on iot devices. *Advances in Neural Information Processing Systems*, 33:11711–11722, 2020. [1](#), [2](#), [6](#), [7](#)
- [42] Tao Lin, Sebastian U. Stich, Luis Barba, Daniil Dmitriev, and Martin Jaggi. Dynamic model pruning with feedback. In *International Conference on Learning Representations*, 2020. [2](#), [6](#)
- [43] Hanxiao Liu, Karen Simonyan, and Yiming Yang. DARTS: Differentiable architecture search. In *ICLR*, 2019. [2](#), [4](#)
- [44] Mark D. McDonnell. Training wide residual networks for deployment using a single bit for each weight. In *International Conference on Learning Representations*, 2018. [7](#), [12](#)
- [45] Fabian Mentzer, Eirikur Agustsson, Michael Tschannen, Radu Timofte, and Luc Van Gool. Practical full resolution learned lossless image compression. In *IEEE/CVF CVPR*, 2019. [8](#)
- [46] Pavlo Molchanov, Stephen Tyree, Tero Karras, Timo Aila, and Jan Kautz. Pruning convolutional neural networks for resource efficient inference. *arXiv preprint arXiv:1611.06440*, 2016. [2](#)
- [47] Max B Paulus, Chris J Maddison, and Andreas Krause. Rao-blackwellizing the straight-through gumbel-softmax gradient estimator. *arXiv preprint arXiv:2010.04838*, 2020. [4](#)
- [48] Hieu Pham, Melody Guan, Barret Zoph, Quoc Le, and Jeff Dean. Efficient neural architecture search via parameters sharing. In *International Conference on Machine Learning*, pages 4095–4104. PMLR, 2018. [2](#)
- [49] Olga Russakovsky, Jia Deng, Hao Su, Jonathan Krause, Sanjeev Satheesh, Sean Ma, Zhiheng Huang, Andrej Karpathy, Aditya Khosla, Michael Bernstein, Alexander C. Berg, and Li Fei-Fei. ImageNet Large Scale Visual Recognition Challenge. *International Journal of Computer Vision (IJCV)*, 115(3):211–252, 2015. [2](#)
- [50] Mark Sandler, Andrew Howard, Menglong Zhu, Andrey Zhmoginov, and Liang-Chieh Chen. Mobilenetv2: Inverted residuals and linear bottlenecks. In *IEEE/CVF CVPR*, pages 4510–4520, 2018. [7](#)
- [51] Pierre Stock, Angela Fan, Benjamin Graham, Edouard Grave, Rémi Gribonval, Herve Jegou, and Armand Joulin. Training with quantization noise for extreme model compression. In *International Conference on Learning Representations*, 2021. [6](#)
- [52] Lucas Theis, Wenzhe Shi, Andrew Cunningham, and Ferenc Huszár. Lossy image compression with compressive autoencoders. *arXiv preprint arXiv:1703.00395*, 2017. [3](#)
- [53] Stefan Uhlich, Lukas Mauch, Fabien Cardinaux, Kazuki Yoshiyama, Javier Alonso Garcia, Stephen Tiedemann, Thomas Kemp, and Akira Nakamura. Mixed precision dnns: All you need is a good parametrization. In *International Conference on Learning Representations*, 2020. [1](#), [2](#), [7](#)

- [54] Alvin Wan, Xiaoliang Dai, Peizhao Zhang, Zijian He, Yuandong Tian, Saining Xie, Bichen Wu, Matthew Yu, Tao Xu, Kan Chen, et al. Fbnetv2: Differentiable neural architecture search for spatial and channel dimensions. In *IEEE/CVF CVPR*, pages 12965–12974, 2020. [2](#), [3](#), [4](#)
- [55] Kuan Wang, Zhijian Liu, Yujun Lin, Ji Lin, and Song Han. HAQ: hardware-aware automated quantization. In *IEEE/CVF CVPR*, 2019. [1](#), [2](#), [7](#)
- [56] Tianzhe Wang, Kuan Wang, Han Cai, Ji Lin, Zhijian Liu, Hanrui Wang, Yujun Lin, and Song Han. Apq: Joint search for network architecture, pruning and quantization policy. In *IEEE/CVF CVPR*, June 2020. [1](#), [2](#), [6](#), [7](#)
- [57] Bichen Wu, Xiaoliang Dai, Peizhao Zhang, Yanghan Wang, Fei Sun, Yiming Wu, Yuandong Tian, Peter Vajda, Yangqing Jia, and Kurt Keutzer. Fbnet: Hardware-aware efficient convnet design via differentiable neural architecture search. In *IEEE/CVF CVPR*, pages 10734–10742, 2019. [2](#), [4](#)
- [58] Haichuan Yang, Shupeng Gui, Yuhao Zhu, and Ji Liu. Automatic neural network compression by sparsity-quantization joint learning: A constrained optimization-based approach. In *IEEE/CVF CVPR*, pages 2178–2188, 2020. [1](#), [2](#), [6](#), [7](#)
- [59] Tien-Ju Yang, Yu-Hsin Chen, and Vivienne Sze. Designing energy-efficient convolutional neural networks using energy-aware pruning. In *IEEE/CVF CVPR*, pages 5687–5695, 2017. [2](#)
- [60] Jianbo Ye, Xin Lu, Zhe Lin, and James Z. Wang. Rethinking the smaller-norm-less-informative assumption in channel pruning of convolution layers. In *International Conference on Learning Representations*, 2018. [2](#)
- [61] Haibao Yu, Qi Han, Jianbo Li, Jianping Shi, Guangliang Cheng, and Bin Fan. Search what you want: Barrier penalty nas for mixed precision quantization. *arXiv preprint arXiv:2007.10026*, 2020. [2](#)
- [62] Sergey Zagoruyko and Nikos Komodakis. Wide residual networks. In Edwin R. Hancock Richard C. Wilson and William A. P. Smith, editors, *Proceedings of the British Machine Vision Conference (BMVC)*, pages 87.1–87.12. BMVA Press, September 2016. [7](#)
- [63] Aojun Zhou, Anbang Yao, Yiwen Guo, Lin Xu, and Yurong Chen. Incremental network quantization: Towards lossless cnns with low-precision weights. *International Conference on Learning Representations*, 2017. [6](#)
- [64] Michael Zhu and Suyog Gupta. To prune, or not to prune: exploring the efficacy of pruning for model compression. *arXiv preprint arXiv:1710.01878*, 2017. [6](#)

### A. Proof of Lemma 3.1

*Proof.* We know that  $p(\mathcal{E}(\{z\}) \neq e^*)$  must be 0. But if  $\mathcal{E}(\{\gamma(\pi)\}) \neq e^*$ ,  $p(\mathcal{E}(\{z\}) \neq e^*) > 0$ , which is a contradiction.  $\square$

### B. Proof of Lemma 3.2

*Proof.* If there is a  $\pi_j$  which is not one-hot, then the following configuration sample has non-zero probability:

- $z_j^s \neq s_j^{s'}$
- $z_k^s = z_k^{s'} \forall k \neq j$

Since we assumed that  $\mathcal{L}_{\mathcal{E}}(\{z\}) = 0$ , Lemma 3.1 gives that  $\mathcal{E}(\{z^s\}) = e^* = \mathcal{E}(\{z^{s'}\})$ . But this is a contradiction since we assumed there are no decisions for which two options have the same efficiency.  $\square$

### C. Derivation of entropy bound

The entropy bound in (3) can be derived as follows:

$$H(Q(\theta, b, r) \odot m) \times \|w\|_0 \quad (10)$$

$$\leq (H(Q(\theta, b, r)) + H(m)) \times \|w\|_0 \quad (11)$$

$$\leq (b + \underbrace{H(m)}_{-s \log_2 s - (1-s) \log_2 (1-s)}) \times \|w\|_0 \quad (12)$$

where the first inequality follows from the fact that the entropy of a product of RVs is bounded by the sum of their entropies and the second bound follows from the fact that  $Q(\theta, b, r)$  costs at most  $b$  bits per element to encode.

### D. CIFAR100 experiment settings

We run the search for 200 epochs, annealing  $\tau$  from 0.66 to 0.1 using an exponential schedule. We use SGD for  $\theta$  with learning rate annealed from 0.1 to  $1e-4$  using a cosine schedule and we use ADAM for  $\{\pi\}$  with a constant learning rate of  $1e-3$ . We increase  $\vartheta$  from 0 to 0.5 using a linear schedule and we increase  $\zeta^t$  from 0.1 to 1 using a linear schedule. We initialize the search by running a warmup stage for 50 epochs where we use SGD for  $\theta$  with learning rate annealed from 0.1 to  $1e-4$  using a cosine schedule,  $\tau$  is annealed from 0.66 to 0.1 using an exponential schedule,  $\{\pi\}$  is not learned, and  $\vartheta = 0$ . During both warmup and search, we set  $\kappa = K$  for all width decisions and  $\kappa = 2$  for all quantization and sparsity decisions.

To finetune the discovered models, we run stage 1 for 254 epochs using SGD and cosine decay with restarts learning rate schedule, cycling between 0.1 and  $1e-4$  at intervals which double after every cycle and beginning with a cycle of 2 epochs. We run stage 2 for 60 epochs, annealing the learning rate from 0.1 to  $1e-4$  using a cosine schedule and

	Top1 acc. (%)	Model size (MB)
UDC	<b>79.24</b>	<b>0.553</b>
Gong et al. [26]	77.84	0.57
UDC	<b>79.71</b>	<b>0.705</b>
Gong et al. [26]	78.73	0.76
McDonnel, [44]	76.26	1.02

Table 5. Detailed CIFAR100 results comparing compressed model size versus accuracy for UDC against SOTA algorithms.

then we run stage 3 for 30 epochs, annealing the learning rate from  $1e-4$  to 0 using a cosine schedule. We use distillation with a teacher model whose architecture is WRN 20-10. For data augmentation, we use horizontal flipping, random crop with a size of 4, and cutout with a size of 18. We use  $\ell_2$  regularization with coefficient  $5e-4$ . We disable learning of batchnorm scale and offset parameters [44].

Table 5 presents the detailed experimental results for the CIFAR100 experiments.

### E. ImageNet experiment settings

We use the same search settings as for the CIFAR100 experiments. To finetune the discovered models, we run stage 1 for 126 epochs using SGD and cosine decay with restarts learning rate schedule, cycling between 0.1 and  $1e-4$  at intervals which double after every cycle and beginning with a cycle of 2 epochs. We run stage 2 for 60 epochs, annealing the learning rate from 0.1 to  $1e-4$  using a cosine schedule and then we run stage 3 for 30 epochs, annealing the learning rate from  $1e-4$  to 0 using a cosine schedule. For the 0.5 and 1MB target experiments, we use distillation with a teacher model whose architecture is MobileNetV2. We do not use distillation for the 1.25MB target experiment. For data augmentation, we use the standard ImageNet data pipeline [19], as well as horizontal flipping and label smoothing with smoothing coefficient 0.1. We use  $\ell_2$  regularization with a coefficient of  $1e-4$ .

Table 6 shows the detailed ImageNet results.

### F. Super Resolution experiment settings

We run the search for 300 epochs, with constant  $\tau$  set to 0.1. We use ADAM for  $\theta$  with learning rate annealed from  $1e-4$  to  $1e-5$  using a cosine schedule and ADAM as well for  $\{\pi\}$  with a constant learning rate of  $1e-3$ . We keep  $\vartheta$  constant to 0.25 and we increase  $\zeta^t$  from 0.1 to 1 using a cosine schedule.

Table 7 provides detailed results for the super resolution experiment.

	Top1 acc. (%)	Model size (MB)
UDC	<b>64.094</b>	<b>0.5</b>
MCUNet [41]	63.5	0.67
UDC	<b>67.164</b>	<b>0.9</b>
MCUNetV2 [40]	64.9	0.99
Choi et al., [17]	64.1	0.94
UDC	<b>71.562</b>	<b>1.27</b>
Choi et al., [17]	65.8	1.35
Lin et al., MCUNet [41]	70.7	1.57
Gong et al., [26]	68.38	1.44
Uhlich et al., [53]	69.74	1.55

Table 6. Detailed ImageNet experimental results, comparing compressed model size versus accuracy for UDC and SOTA algorithms.

	PSNR (dB)	MAC (x1e6)
UDC	<b>35.13</b>	75.4
Bharadwaj et al., [12]	35.01	<b>72.9</b>
UDC	35.21	<b>85</b>
UDC	<b>35.29</b>	105.8
Bharadwaj et al., [12]	35.2	110.6

Table 7. Detailed super resolution experiment results comparing UDC to a SOTA efficient super resolution algorithm.

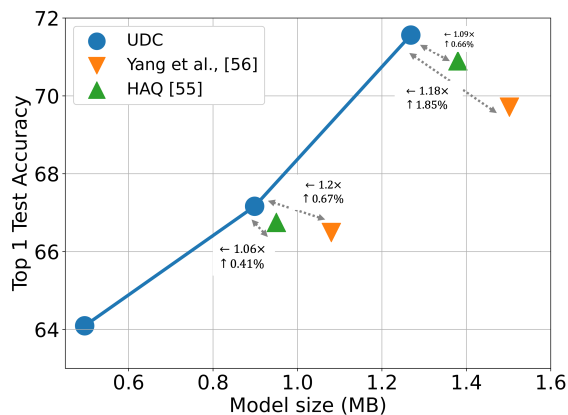


Figure 8. ImageNet test set accuracy vs. compressed model size.

## G. Comparison to non-uniform quantization approaches

We compare UDC to approaches which employ non-uniform quantization in Fig. 8. UDC is Pareto-dominant even though it uses uniform quantization and can be deployed on MCUs/NPUs with integer math whereas the other approaches cannot.

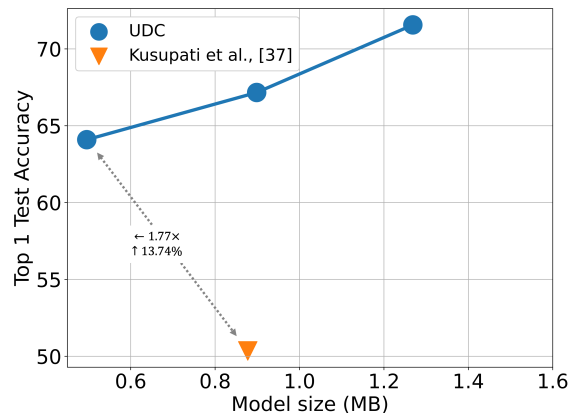


Figure 9. ImageNet test set accuracy vs. compressed model size.

## H. Comparison to approaches which only do unstructured pruning

We also compare UDC to a SOTA unstructured pruning algorithm [37] in Fig. 9. As the results show, UDC generates much more accurate models.

## I. Visualization of design choices

We provide a visualization of the design choices made by UDC for the ImageNet experiments in Fig. 10-12.

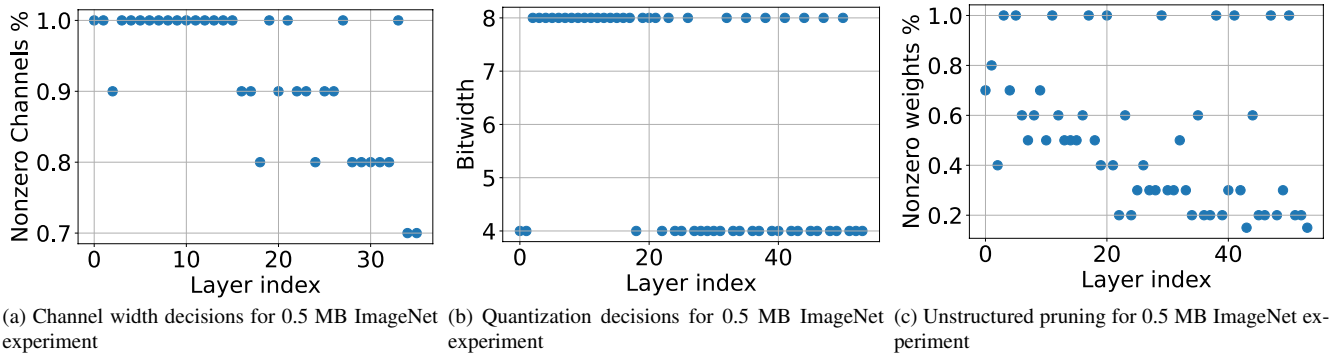


Figure 10. Model decisions for 0.5MB ImageNet experiment.

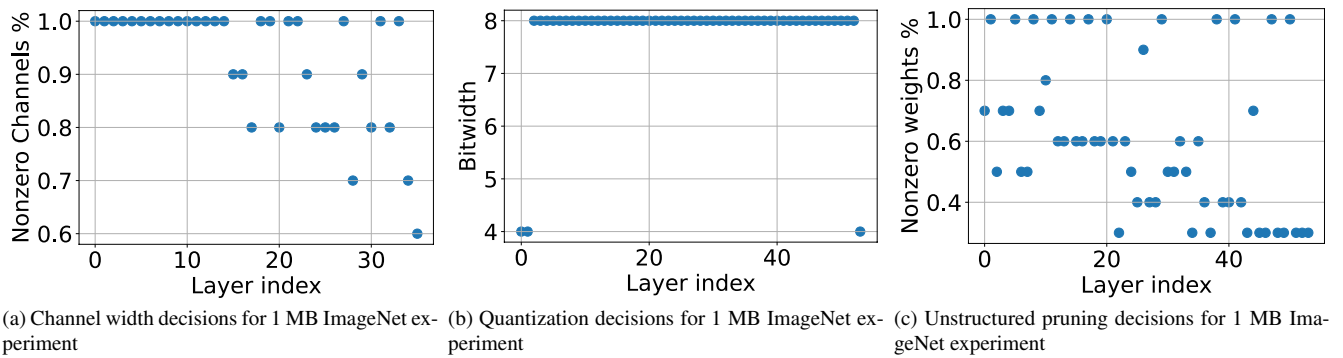


Figure 11. Model decisions for 1 MB ImageNet experiment.

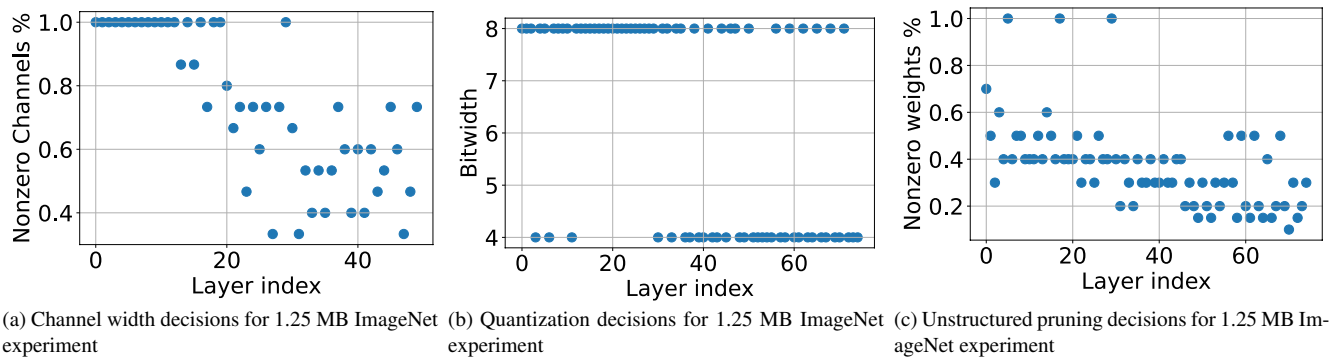


Figure 12. Model decisions for 1.25 MB ImageNet experiment.